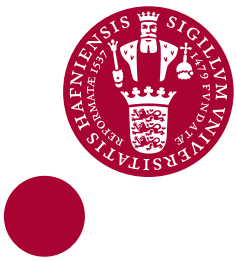

Using Rigid Microplate Motions to Detect the Stress Buildup Preceding Large Earthquakes

A Feasibility Test Based on Synthetic Models

Martin de Blas, Juan; Iaffaldano, Giampiero

Published in:
Journal of Geophysical Research: Biogeosciences

DOI:
10.1029/2019JB018175

Publication date:
2019

Document version
Publisher's PDF, also known as Version of record

JGR Solid Earth

RESEARCH ARTICLE
10.1029/2019JB018175

Using Rigid Microplate Motions to Detect the Stress Buildup Preceding Large Earthquakes: A Feasibility Test Based on Synthetic Models

Juan Martin de Blas[1] and Giampiero Iaffaldano[1]

[1]Department of Geosciences and Natural Resource Management, University of Copenhagen, Copenhagen, Denmark

Key Points:
- It appears feasible to link the charge phase of large earthquakes to temporal changes in rigid microplate motions
- We built synthetic simulations of the dynamics of a microplate affected by the charge of one large earthquake and many smaller ones
- We assessed the impact of the viscosity of the asthenosphere, size of the microplate, and microplate geometry

Supporting Information:
- Supporting Information S1

Correspondence to:
J. Martin de Blas,
jmb@ign.ku.dk

Citation:
Martin de Blas, J. I., & Iaffaldano, G. (2019). Using rigid microplate motions to detect the stress buildup preceding large earthquakes: A feasibility test based on synthetic models. *Journal of Geophysical Research: Solid Earth*, *124*, 13,468–13,485. https://doi.org/10.1029/2019JB018175

Received 11 JUN 2019
Accepted 10 DEC 2019
Accepted article online 12 DEC 2019
Published online 28 DEC 2019

Abstract Assessing the temporal evolution of stresses along seismogenic faults is typically done by combining geodetic observations collected near the locations of previous large earthquakes with modeling of the interseismic, coseismic, and postseismic deformation. Here we explore whether it is feasible to link the charge phase of large earthquakes to rigid microplate motions, which can be inferred from geodetic observations that are instead collected further away from crustal faults. We use numerical simulations of the dynamics and associated kinematics of an idealized, rigid microplate subject to stress buildups and drop-offs from a series of earthquakes. Simulations span the charging cycle of a single $6.5 < M_W \leq 8$ earthquake. Several $M_W \leq 6.5$ earthquakes distributed according to the Gutenberg-Richter law occur meanwhile. We use large ensembles of simulations featuring randomly-generated earthquake hypocenters and make statistical assessments of the fraction of model time needed for the microplate motions to depart from the initial one to a degree that is larger than typical geodetic uncertainties and for at least 90% of the remaining time before the large earthquake occurs. We find such a fraction (i) to be only one tenth in simulations that do feature a large earthquake, (ii) to be longer in simulations that do not, and (iii) to remain small for realistic microplate geometries and asthenosphere viscosity/thickness values. Our inferences hold also when we simulate geodetic time series shorter than the large earthquake cycle and even when we assume that only half of the stress buildup affects the microplate rigid motion.

1. Introduction

Large earthquakes along tectonic margins result from the long-term relative motions between lithospheric plates. These motions cause crustal deformation, and the consequent accrual of energy is eventually released through seismic events. Assessing the seismic hazard along tectonic faults relies significantly on earthquake catalogs. Such an approach carries the expectation that future earthquakes will occur close to the locations of previous seismic events (e.g., Stein & Wysession, 2003). The advent of geodesy in the geosciences (e.g., Dixon, 1991) allowed time-dependent monitoring of the deformation in the vicinity of tectonic margins through techniques such as Global Navigation Satellite Systems, Satellite Laser Ranging, and Very Long Baseline Interferometry. The Global Positioning System (GPS) is currently widely used in order to determine position time series with a millimeter-level precision (e.g., Bock & Melgar, 2016) and allows detecting the interseismic deformation, as well as the coseismic and postseismic crustal motions (e.g., Freed et al., 2006; Meade & Loveless, 2017). Currently, the assumption built in earthquake models—that is, that future events will tend to occur near previous ones—drives the deployment of permanent/campaign GPS networks mainly in the vicinity of recently-ruptured faults (e.g., Bock & Melgar, 2016; LaFemina et al., 2009; Reilinger et al., 2006; Rui & Stamps, 2019; Symithe et al., 2015; Tregoning, 2002; Wallace et al., 2004). Importantly, it is commonly accepted that the energy accrued across crustal faults due to plate motions during the preseismic phase affects only the deformation in the vicinity of the fault and not the plate motions that caused deformation in the first place. In other words, it is assumed that the seismic cycle does not impact on rigid plate motions. Such an assumption is well justified if one considers how large the torques needed to change plate motions are. To first degree, they scale with the basal area of plates—because processes affecting plate motions need to overcome the Couette-type resistance at the plate base (e.g., Stotz et al., 2018)—and feature values in the order of 10^{25} to 10^{26} *Nm* for the largest tectonic plates (e.g., Iaffaldano, 2014). Stresses associated with large earthquakes (e.g., Ben-Zion, 2008; Kanamori, 1978) are not capable of yielding such large torques.

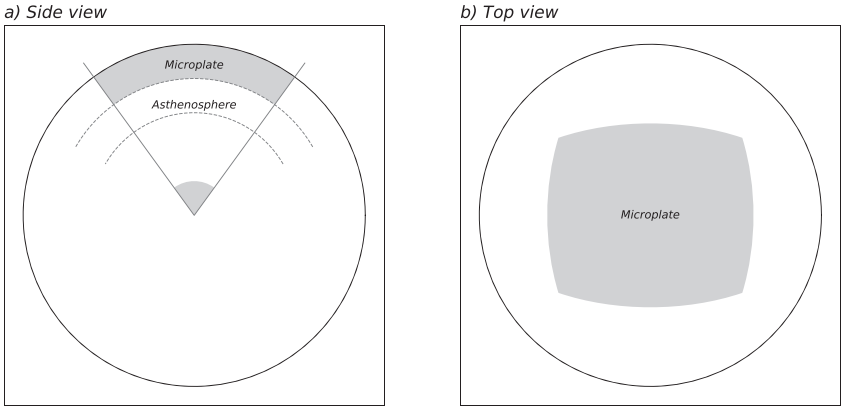

Figure 1. Microplate geometry in side (a) and top (b) views. Plate size is exaggerated for easiness of visualization.

The recent discovery of tectonic units that move rigidly but are smaller than lithospheric plates—referred to as microplates (Wallace et al., 2005)—adds a different perspective to this inference. Torques needed to change the motions of microplates are a few orders of magnitude smaller than the estimates above and thus fall within the range of what large earthquakes are indeed capable of providing. In principle, this introduces the possibility that the stress buildup occurring on microplate margins and leading to large earthquakes may affect not only crustal deformation in the vicinity of the future rupture area but also the rigid motion of the entire microplate. Here we take this view and explore, through simulations of plate dynamics and associated kinematics, whether large ($6.5 \leq M_W \leq 8$) earthquakes charging along the boundaries of an idealized microplate may impact on its rigid motion. The model time period of each of our simulations spans the charge cycle of one single large earthquake. Simulations also feature the occurrence of smaller ($3.5 \leq M_W < 6.5$) earthquakes whose number and magnitude follow the Gutenberg-Richter empirical law and that are randomly distributed in model time and space. From the stresses associated with each earthquake, we calculate torque variations and consequent microplate Euler-vector changes through model time. By analyzing thousands of randomly-generated simulations, we explore whether the charge phase of large earthquakes carries any kinematic signatures that are potentially visible relatively early on in real records of microplate motions.

2. Concepts and Methods

We set up synthetic simulations for the temporal evolution of microplate dynamics and kinematics. We take a model microplate shaped like a squared portion of a 3-D spherical shell—that is, the volume cut by intersecting a spherical shell whose outer radius is equal to Earth's radius with a pyramid pointing to the sphere center (Figures 1a and 1b). The microplate size (i.e., lateral extent) is a free parameter of the problem. Furthermore, we also model the presence of a viscoelastic asthenosphere separating the microplate from the lower part of the upper mantle (region between dashed lines in Figure 1a). Viscosities of the asthenosphere (μ_a) and the lower part of the upper mantle (μ_m) are also free parameters that we assume to be uniform within their own domains. Instead, the asthenosphere thickness (D_a) is determined on the basis of the work of Paulson and Richards (2009) and Richards and Lenardic (2018), who modeled long-wavelength post-glacial rebound data to infer that $\mu_m/\mu_a \propto D_a^{-3}$. At the initial model time, the Euler vector describing the microplate rigid motion features a randomly-generated Euler pole that can fall as far as 1,000 km away from the microplate margins. The angular velocity at the initial model time is also randomly selected within the range from 1 to 8 °/Myr. These features are in line with geodetic measurements of, for instance, the Anatolian, South Bismark, New Zealand, Vanuatu, and Marianas microplate motions (McClusky et al., 2000; Wallace et al., 2005).

The model microplate is subject to stress variations associated with the slow charge and sudden discharge of one large earthquake randomly located along the microplate margins and whose moment magnitude (M_W) is randomly selected in range 6.5 to 8. The upper limit of such a range approximates well the magnitude of the largest earthquakes recorded along the margins of the microplates mentioned above (USGS and NOAA earthquake catalogs). The model time of each simulation represents thus the period of time it

takes to slowly charge and suddenly discharge one such large earthquake. This may be thought as the recurrence time of $6.5 \leq M_W \leq 8$ earthquakes—that is, a few hundred years at most. Meanwhile, several smaller (i.e., $3.5 \leq M_W < 6.5$) earthquakes are also cast in the simulations and occur randomly in model time, location, and depth along the microplate margins. We impose that the whole set of earthquakes follows the Gutenberg-Richter empirical law (Gutenberg & Richter, 1944)—that is, $log_{10}(N_M) = a - b \cdot M$, where N_M is the number of earthquakes whose magnitude is at least M, while a and b are numerical parameters specific to the tectonic region of focus. In particular, b is typically close to 1 but is observed to vary between ~0.8 and ~1.2 (e.g., Godano et al., 2014; Nishikawa & Ide, 2014), possibly as a result of a range of local tectonic conditions (e.g., Dal Zilio et al., 2018; Tormann et al., 2015). In a set of earthquakes that follows the Gutenberg-Richter empirical law, the number of events featuring $M_W \geq m$ is 10^b times the number of events featuring $M_W \geq m + 1$. The synthetic scenarios simulated here feature one single event where $M_W \geq 6.5$. Accordingly, there are 10^b events where $M_W \geq 5.5$, 10^{2b} events where $M_W \geq 4.5$, and 10^{3b} events where $M_W \geq 3.5$. Furthermore, the model time it takes to charge an earthquake of $M_W = m$ is $\sim 10^{-b}$ times the model time it takes to charge an earthquake of $M_W = m + 1$. For instance, selecting $b = 1$ means that the whole set of earthquakes features a total of $10^{3b} = 1,000$ events. At any point in model time, the microplate will be subject to the charge of only one single earthquake featuring $M_W \geq 6.5$ (the largest in the synthetic set), while several smaller ones (i) might be charging meanwhile, (ii) will have already charged and discharged, or (iii) are yet to begin charging.

We subdivide the whole simulated model period into $n_s = 4 \cdot int\ (10^{3b})$ model time steps, where *int* indicates the integer part. The slow charge phase of the single largest earthquake spans $(n_s - 1)$ model time steps, while its sudden discharge phase only takes the very last model time step. The charge and discharge times for the synthetic earthquakes whose M_W is smaller than the largest one within the set span a number of model time steps $n_e < n_s$ dictated by the Gutenberg-Richter scaling illustrated above. Also for these earthquakes, the slow charge phase takes $(n_e - 1)$ time steps to be accomplished, while the sudden discharge occurs within a single time step. The total number of time steps in each simulation is such that the charge and subsequent discharge phases of any of the earthquakes featuring the smallest M_W within the set span at least four model time steps. If one indicated with T the recurrence time of the largest earthquake within the set, then each model time step represents an interval of time equivalent to $T/[4 \cdot int\ (10^{3b})]$. For instance, if one assumes $T = 100$ yr, then each model time step represents an interval between $6 \cdot 10^{-3}$ yr (assuming $b = 1.2$) and $1 \cdot 10^{-1}$ yr (assuming $b = 0.8$). Instead, if one considers $T = 300$ yr, then the model time step represents an interval between $1.8 \cdot 10^{-2}$ and $3 \cdot 10^{-1}$ yr.

Next, we assess the impact of each earthquake onto the microplate dynamics through model time. We do so by making quantitative estimates of (i) the amount of stress $\Delta\sigma_e$ built during the slow charge phase of an earthquake on the future rupture area S and later released during the earthquake. (ii) The torque variation $\Delta\vec{M}_e$ (in the following, $\vec{M}$ is generically used to indicate a torque) associated with $\Delta\sigma_e$ experienced by the microplate. (iii) The microplate Euler-vector variation $\Delta\vec{\omega}_e$ (in the following, $\vec{\omega}$ is generically used to indicate an Euler vector) caused by $\Delta\vec{M}_e$. We illustrate in the following subsections the way in which we make each of these estimates.

2.1. S and $\Delta\sigma_e$ Associated With Synthetic Earthquakes

We resort to empirical relationships that map M_W into the size of the rupture area along the microplate margins and the associated stress, which builds up slowly and drops down suddenly. We start from the following relationships (see Stein & Wysession, 2003, and references therein for a detailed account of these relationships):

$$M_W = 5.08 + 1.16 \log\,(L), \tag{1}$$

where L is a characteristic length of the rupture area expressed in km. Furthermore,

$$M_W = \frac{\log M_0}{1.5} - 10.73, \tag{2}$$

where M_0 is the seismic moment. Lastly,

$$\Delta\sigma_e = \frac{2}{\pi}\frac{M_0}{l^2 L}, \tag{3}$$

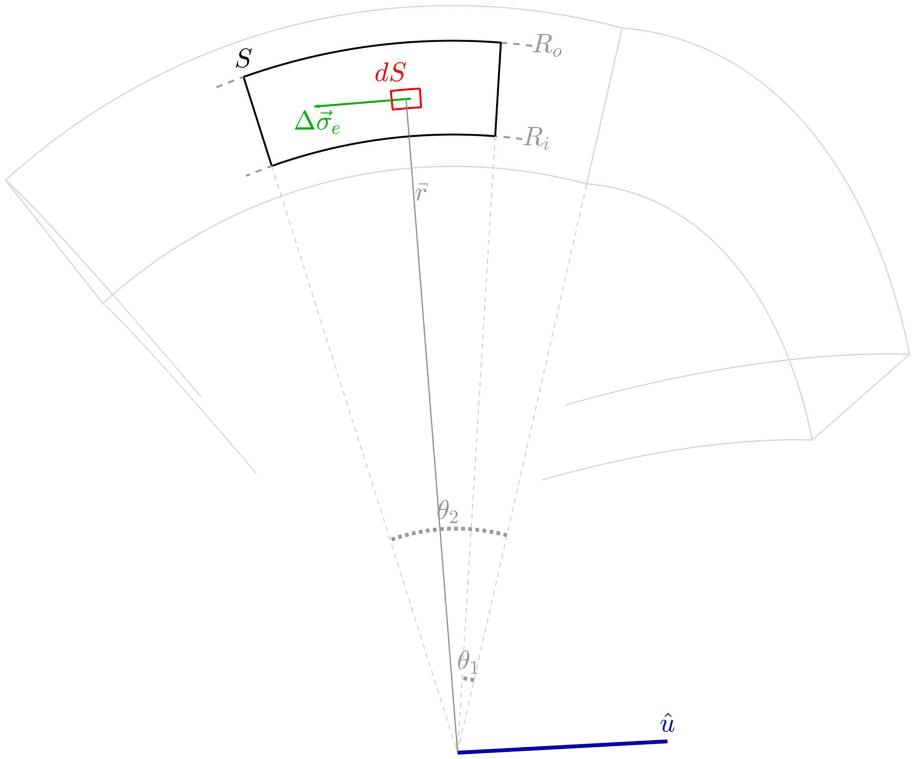

Figure 2. Sketch in support of the calculation of torques arising from the stress associated with a synthetic earthquake ($\Delta\vec{\sigma}_e$, in green). In gray is the contour of the model microplate, whose front corner has been removed for clarity. In black is an exemplary rupture area S. In red is the rupture area infinitesimal element dS, while $\vec{r}$ is its position vector. In blue is the unit vector $\hat{u}$ of the torque. The origin of position vectors such as $\vec{r}$ is Earth's center.

where $\Delta\sigma_e$ is expressed in dyn/cm^2. Symbols l and L in equation (3) indicate the shortest and longest (i.e., characteristic length) sides—expressed in cm—of a rupture area assumed to be rectangular. Thus, we assume for simplicity that $l = L/2$ so that equation (1) alone allows us to link S to M_W. Equation (3) becomes

$$\Delta\sigma_e = \frac{8}{\pi}\frac{M_0}{L^3}. \tag{4}$$

We invert equations (1) and (2) and substitute them into equation (4) in order to obtain a relationship that expresses $\Delta\sigma_e$ as a function of M_W. In our simulations, the stress variation $\Delta\sigma_e$ associated with each synthetic earthquake builds up upon the microplate during the slow charge phase through a series of $(n_e - 1)$ equally-spaced stepwise increases. Each of them feature a stress increase of $\Delta\sigma_e/(n_e - 1)$. After the charge phase, a sudden stepwise stress drop of $-\Delta\sigma_e$ acts upon the microplate within a single model time step in order to release the stress accrued during the charge phase. Thus, each synthetic earthquake generates two stress variations equal in magnitude but opposite in direction: The first one grows slowly during the charge phase, at increments of $\Delta\sigma_e/(n_e - 1)$, while the second one acts suddenly (i.e., within one single model time step) upon the microplate.

2.2. $\Delta\vec{M}_e$ Associated With Synthetic Earthquakes

For each synthetic earthquake, both the stress vector (referred to as $\Delta\vec{\sigma}_e$, where $|\Delta\vec{\sigma}_e| = \Delta\sigma_e$ from Section 2.1) and the rupture area S where the stress buildups lie within the plane defined by the microplate margin (see Figure 2). Since in real tectonic settings the charge of earthquakes is determined by the direction of relative plate motions along each of the microplate margins, we assume that all earthquakes occurring on a specific side of the microplate charge in the same direction. Such a direction changes randomly as one moves from one microplate margin to another and is reset randomly within each simulation. By construction of the idealized microplate, the plane containing $\Delta\vec{\sigma}_e$ and S is a plane that cuts Earth into two hemispheres (i.e., a plane whose intersection with Earth yields a great circle; see Figures 1a and 2). This means that one can identify the rupture area S using polar coordinates within such a plane. That is, S can be identified by

taking the polar radius r between an outer value R_o and an inner value R_i, and the polar angle θ between θ_1 and θ_2. If one were to take θ in range 0 to 2π and r in range 0 to Earth's radius R_E, then the area would simply be $\pi {R_E}^2$. The infinitesimal rupture area is therefore $dS = r \cdot d\theta \cdot dr$ and can be located using the generic position vector $\vec{r}$ (see Figure 2). We assume for simplicity that all margins of the model microplate are dominated by a pure strike-slip regime, which implies that $\Delta\vec{\sigma}_e$ is tangential to a small circle that also lies within the microplate-margin plane and that is normal to the position vector $\vec{r}$ of dS (see Figure 2)—that is, $|\vec{r} \times \Delta\vec{\sigma}_e| = r \cdot \Delta\sigma_e$.

The product $\Delta\vec{\sigma}_e \cdot dS$ represents the infinitesimal force arising from the stress that is slowly built during the charge phase and suddenly released during a synthetic earthquake. The associated infinitesimal torque variation upon the microplate is thus $\vec{r} \times (\Delta\vec{\sigma}_e \cdot dS)$. On any of the four microplate margins, the cross product $\vec{r} \times \Delta\vec{\sigma}_e$ is always directed along an axis that is normal to the plane mentioned above (see exemplary blue axis in Figure 2). The unit vector of such an axis (û) can be calculated by taking the norm of the cross product between the position vectors that locate the two vertices of the microplate margin. Thus, infinitesimal torque variations associated with all earthquakes occurring on a specific microplate margin are oriented like û, such that $\vec{r} \times (\Delta\vec{\sigma}_e \cdot dS) = (r \cdot \Delta\sigma_e \cdot dS) \cdot \hat{u}$. Consequently, the torque variation associated with a specific synthetic earthquake is

$$\Delta\vec{M}_e = \int_S \vec{r} \times (\Delta\vec{\sigma}_e \cdot dS) = \hat{u} \cdot \int_{R_i}^{R_o} \int_{\theta_1}^{\theta_2} \Delta\sigma_e \cdot r \cdot dS, \tag{5}$$

which yields

$$\Delta\vec{M}_e = \hat{u} \cdot \int_{R_i}^{R_o} \int_{\theta_1}^{\theta_2} \Delta\sigma_e \cdot r \cdot r \; d\theta \; dr = \hat{u} \cdot \Delta\sigma_e \int_{R_i}^{R_o} r^2 dr \int_{\theta_1}^{\theta_2} d\theta. \tag{6}$$

Therefore,

$$\Delta\vec{M}_e = \hat{u} \cdot \left(\frac{1}{3} \; \Delta\sigma_e \; (\theta_2 - \theta_1) \; (R_o^3 - R_i^3) \right). \tag{7}$$

As for $\Delta\sigma_e$, the torque variation $\Delta\vec{M}_e$ associated with each synthetic earthquake builds up upon the microplate during the slow charge phase through a series of $(n_e - 1)$ increases, each featuring a torque increment equal to $\Delta\vec{M}_e/(n_e - 1)$. After the charge phase, a sudden torque change equal to $-\Delta\vec{M}_e$ acts upon the microplate within a single model time step. Thus, we simulate each synthetic earthquake using two torque variations equal in magnitude but opposite in direction: The first one grows slowly during the charge phase, at increments of $\Delta\vec{M}_e/(n_e - 1)$, while the second one acts suddenly upon the microplate.

2.3. $\Delta\vec{\omega}_e$ Associated With $\Delta\vec{M}_e$

Under the perfectly-rigid approximation, forces and stresses applied to plates are transferred to the underlying asthenosphere by virtue of plate rigidity. In the context of this study, this means that plate-motion variations arising from the slow increase and sudden drop of stress associated with each earthquake can be inferred quantitatively by balancing these stresses with response of the underlying asthenosphere. Over geological time scales, such a response is that of a highly-viscous fluid. However, at the time scales of the cycle of large earthquakes, one should account for the viscoelastic character of the asthenosphere, whereby its response is initially that of an elastic body but approaches through time the one of a perfectly-viscous fluid. Such transition in rheological behavior occurs over an interval of time comparable to the Maxwell time $T_M = \mu_a/E_a$—where E_a is the asthenosphere Young's modulus. Here we take μ_a in range $5 \cdot 10^{19}$ to $1 \cdot 10^{20}$ (e.g., Forte et al., 2010; Paulson & Richards, 2009). For E_a in range $1.4 \cdot 10^{11}$ to $1.6 \cdot 10^{11}$ Pa (e.g., Turcotte & Schubert, 2002), T_M is around one to two decades. On this basis, we derive an expression for the Euler vector variation $\Delta\vec{\omega}_e$ associated with $\Delta\vec{M}_e$ under viscoelastic conditions as follows: First, in 2.3.1, we derive the expression of $\Delta\vec{\omega}_e$ under the assumption of perfectly-viscous behavior of Earth's asthenosphere, which represents the long-term velocity response to stresses upon the microplate. Next, in 2.3.2, we apply the Burgers' body model—whereby the response of a viscoelastic body to applied strains and stresses is described as that of a Kelvin unit (a dashpot and a spring connected in parallel) connected in series to a Maxwell unit (a dashpot and a spring connected in series)—to Earth's asthenosphere in order to express the temporal evolution of the microplate motion in response to a series of short, closely-spaced stepwise stress increments (i.e., a stress ramp) followed by a sudden stepwise stress drop. For simplicity, we illustrate this in 1-D linear

geometry, but the same rheological arguments apply to the case of 3-D spherical geometry. Lastly, in 2.3.3, we mirror the characteristics of the viscoelastic temporal evolution of kinematics into the perfectly-viscous solution, in order to express the 3-D spherical viscoelastic response of the microplate motion to the stress ramp/drop associated with synthetic earthquakes.

2.3.1. $\Delta\vec{\omega}$ Associated With $\Delta\vec{M}$—Case of a Perfectly Viscous Asthenosphere

We resort to expressions that link torque variations to rigid Euler-vector changes under the assumption that Earth's asthenosphere behaves as a perfectly-viscous fluid (Iaffaldano & Bunge, 2015; Stotz et al., 2018). Euler vectors describing the rigid motions of tectonic plates arise from the balance of torques acting upon them. Torques can be associated with shallow tectonic processes or with basal shear stresses exerted by Earth's asthenospheric flow at the lithosphere base. Under the assumption of perfectly-viscous conditions, the balance of these torques would occur almost instantaneously, relative to geological timescales (e.g., Iaffaldano & Bunge, 2015). This means that at any point in time t, it is

$$\vec{M}(t) + \vec{M}_b(t) = 0, \tag{8}$$

where $\vec{M}(t)$ is the sum of all shallow-seated torques acting upon a plate at t, while $\vec{M}_b(t)$ is the summation of torques arising from stresses tangent to the plate base (i.e., basal shear stresses, referred to in the following as $\vec{\sigma}_b$). That is,

$$\vec{M}_b(t) = \int_A \vec{r} \times \vec{\sigma}_b(\vec{r}, t) \cdot dA, \tag{9}$$

where A is the plate basal area and dA is its generic infinitesimal at position $\vec{r}$. If one considers two points in time, t_1 and t_2, that are sufficiently close to each other so that the plate basal area does not change yet distant enough that the torque balance is reachieved, then the torque balances at t_1 and t_2 are

$$\vec{M}(t_1) + \int_A \vec{r} \times \vec{\sigma}_b(\vec{r}, t_1) \cdot dA = 0, \tag{10}$$

and

$$\vec{M}(t_2) + \int_A \vec{r} \times \vec{\sigma}_b(\vec{r}, t_2) \cdot dA = 0. \tag{11}$$

Taking the difference of these equations yields

$$\vec{M}(t_2) - \vec{M}(t_1) + \int_A \vec{r} \times \vec{\sigma}_b(\vec{r}, t_2) \cdot dA - \int_A \vec{r} \times \vec{\sigma}_b(\vec{r}, t_1) \cdot dA = 0, \tag{12}$$

or

$$\Delta\vec{M}(t_1, t_2) = \int_A \vec{r} \times [\vec{\sigma}_b(\vec{r}, t_1) - \vec{\sigma}_b(\vec{r}, t_2)] \cdot dA, \tag{13}$$

where $\Delta\vec{M}(t_1, t_2) = \vec{M}(t_2) - \vec{M}(t_1)$.

The term on left-hand side represents the variation of shallow-seated torques experienced by the plate from t_1 to t_2. Instead, the term on right-hand side expresses the change in shear stresses acting at the plate base. Stresses are the product of the viscosity and the strain rate. In the specific case of $\vec{\sigma}_b$, one should multiply the asthenosphere viscosity μ_a with the shear-strain rate at the plate base, which can be obtained by taking the radial gradient of the asthenospheric flow that is tangential to the plate base (in the following, we refer to such flow as $\vec{v}_a$). The latter one is the solution to the equation of dynamic balance of viscous flow (see Davies, 1999, for more details), which expresses in mathematical terms the notion that shear flow in the asthenosphere can be driven (i) by plate motions on top (commonly referred to as Couette-type flow), (ii) by pressure gradients within the asthenosphere/mantle (commonly referred to as Poiseuille-type flow), or (iii) by a combination of both. The Couette-type flow can always be expressed as $\vec{v}_p(\vec{r}, t) \cdot h/D_a$, where $\vec{v}_p$ is the rigid plate motion at the plate-base position $\vec{r}$, while h is a generic depth at $\vec{r}$, within the asthenosphere. Such an expression builds on the reasonable assumption that the Couette-type flow decreases to nearly zero around the asthenosphere bottom due to the large viscosity contrast with the upper mantle. Instead, the Poiseuille-type flow cannot be expressed analytically, although exact solutions exist for several simple cases (e.g., Davies, 1999; Turcotte & Schubert, 2002). We indicate with $\vec{v}_{aP}(\vec{r}, h, t)$ the generic Poiseuille-type flow.

Since the equation describing the dynamic balance of a viscous flow depends linearly on the terms driving Poiseuille- and Couette-type flows, one can always write a generic expression of the asthenospheric flow as a linear combination of the two flow types. That is, $\vec{v}_a(\vec{r},h,t) = \vec{v}_p(\vec{r},t)\cdot h/D_a + \vec{v}_{aP}(\vec{r},h,t)$. Thus, a generic expression for shear stresses at the plate base can be obtained by multiplying the asthenosphere viscosity and the vertical gradient of $\vec{v}_a$ (i.e., its derivative relative to h) calculated at $h = 0$. That is,

$$\vec{\sigma}_b(\vec{r},t) = \mu_a \cdot \left[\frac{d}{dh}\vec{v}_a(\vec{r},h=0,t)\right] = \mu_a \cdot \left[-\frac{\vec{v}_p(\vec{r},t)}{D_a} + \frac{d}{dh}\vec{v}_{aP}(\vec{r},h=0,t)\right], \tag{14}$$

where the negative sign in front of the Couette-type component accounts for the fact that the associated stress always acts as a resisting force upon the plate.

Bunge (2005) showed that patterns of mantle convection, and thus the associated Poiseuille-type flow, change significantly only over time scales longer than 100 Myr. Since this is much longer than the time scales considered in this study, it is reasonable to take $d\vec{v}_{aP}(\vec{r},h,t1)/dh = d\vec{v}_{aP}(\vec{r},h,t2)/dh$. That means that any Poiseuille-type flow underneath the microplate does not change significantly over the recurrence time of a large earthquake. Therefore, substituting equation (14) into (13) yields

$$\Delta\vec{M} = \frac{\mu_a}{D_a}\int_A \vec{r}\times[\vec{v}_p(\vec{r},t_2) - \vec{v}_p(\vec{r},t_1)]\cdot dA. \tag{15}$$

Since rigid plate motions can be expressed through the associated Euler vectors (i.e., $\vec{v}_p(\vec{r},t) = \omega(t)\times\vec{r}$), equation (15) becomes

$$\Delta\vec{M} = \frac{\mu_a}{D_a}\int_A \vec{r}\times[(\vec{\omega}(t_2)\times\vec{r}) - (\vec{\omega}(t_1)\times\vec{r})]\cdot dA, \tag{16}$$

or

$$\Delta\vec{M} = \frac{\mu_a}{D_a}\int_A \vec{r}\times(\Delta\vec{\omega}\times\vec{r})\cdot dA, \tag{17}$$

where $\Delta\vec{\omega} = \vec{\omega}(t_2) - \vec{\omega}(t_1)$ is the Euler-vector temporal change.

The step from equations (15) to (16) implies the assumption that the entire plate basal area moves in a perfectly rigid fashion, so that an Euler-vector description may be adopted. For most of the basal areas of tectonic plates, this is a generally accurate description (e.g., Gordon, 1998). However, regions of the basal area near portions of the microplate margins where the charge phase of earthquakes—particularly large ones—is taking place may represent exceptions. In particular, this is true if one were to adopt the viscoelastic coupling (e.g., Savage & Prescott, 1978) or the strong plastosphere models (e.g., Bourne et al., 1998)—as opposed to the deep shear zone model (e.g., Scholz, 2019)—in order to describe the strain accumulation during the interseismic phase (see Scholz, 2019 for a comprehensive review of these models). At the surface, interseismic deformation can extend inside the microplate as far as ~100 km away from the charging fault (e.g., Shen et al., 1996). This can be taken as an upper limit for the extent inside the microplate basal area of regions that do not follow the rigid Euler-vector description. Thus, one can argue that these regions feature an area that is at most $L\cdot 100\ \mathrm{km}^2$, where L is the rupture length from equation (1) above. For a $M_W = 8$ (the maximum possible in the simulations), L is equal to ~300 km. Therefore, the basal-area region where deviations from the Euler-vector description may occur can be at most ~10% of the total basal area of a microplate whose side length is 550 km and would be only ~2% of the basal area if the side length is 1,100 km. For a $M_W = 7.5$ synthetic earthquake, these percentages decrease to ~4% and ~1%. On this basis, we argue that in practice, the step from 16 to 17 carries a negligible error propagating to the torque-variation assessment.

We indicate with x, y, and z the generic Cartesian components of $\vec{r}$. Similarly, we indicate with $\Delta\omega_x$, $\Delta\omega_y$, and $\Delta\omega_z$ the Cartesian components of $\Delta\vec{\omega}$. It is straightforward to show that the Cartesian components of vectorial equation (17) are

$$\begin{aligned}
\Delta M_x &= \frac{\mu_a}{D_a}\int_A [\Delta\omega_x(y^2+z^2) + \Delta\omega_y(-xy) + \Delta\omega_z(-xz)]dA,\\
\Delta M_y &= \frac{\mu_a}{D_a}\int_A [\Delta\omega_x(-xy) + \Delta\omega_y(x^2+z^2) + \Delta\omega_z(-yz)]dA,\\
\Delta M_z &= \frac{\mu_a}{D_a}\int_A [\Delta\omega_x(-xz) + \Delta\omega_y(-yz) + \Delta\omega_z(x^2+y^2)]dA.
\end{aligned} \tag{18}$$

Since the terms $\Delta\omega_x$, $\Delta\omega_y$, and $\Delta\omega_z$ are constant within each integral, they can be taken outside the integration sign. The set of scalar equations above can then be seen as the following linear transformation

$$\underbrace{\begin{pmatrix}\Delta M_x\\ \Delta M_y\\ \Delta M_z\end{pmatrix}}_{\Delta\vec{M}} = \underbrace{\frac{\mu_a}{D_a}\begin{pmatrix}\int_A(y^2+z^2)dA & -\int_A xydA & -\int_A xzdA\\ -\int_A xydA & \int_A(x^2+z^2)dA & -\int_A yzdA\\ -\int_A xzdA & -\int_A yzdA & \int_A(x^2+y^2)dA\end{pmatrix}}_{\mathbf{C}}\underbrace{\begin{pmatrix}\Delta\omega_x\\ \Delta\omega_y\\ \Delta\omega_z\end{pmatrix}}_{\Delta\vec{\omega}}, \tag{19}$$

or

$$\Delta\vec{M} = \mathbf{C}\Delta\vec{\omega}, \tag{20}$$

where $\mathbf{C}$ is a linear operator that depends on plate geometry and viscosity/thickness of the asthenosphere. $\mathbf{C}$ features $det(\mathbf{C}) = 0$ because of the integral nature of its entries and may thus be inverted so that

$$\Delta\vec{\omega} = \mathbf{C^{-1}}\Delta\vec{M}. \tag{21}$$

By way of example, substituting equations (2), (4), and (7) into (21) indicates that a microplate whose typical length is 550 km would undergo angular-velocity variations of ~0.03 °/Myr when $M_w = 6$, ~0.1 °/Myr when $M_w = 7$, and ~0.5 °/Myr when $M_w = 8$. Instead, for a microplate whose typical length is 800 km, variations amount to ~0.01 °/Myr, ~0.04 °/Myr, and ~0.18 °/Myr, respectively.

2.3.2. Linking the Temporal Evolutions of Plate Motions and Stress Variations—Case of a Viscoelastic Asthenosphere

We make use of a toy problem in order to illustrate the impact of viscoelasticity of Earth's asthenosphere on the temporal evolution of plate motions. Specifically, we resort to the Burgers' model, which is widely applied to simulate the postseismic deformation in the vicinity of subduction mantle wedges (see Govers et al., 2018, for a review). For instance, Pollitz et al. (2006) and Broerse et al. (2015) utilized the predicted Burgers's body response to a sudden strain in order to describe the viscoelastic deformation within the mantle wedge near part of the Australian/Eurasian plate margin following the 2004 Sumatra-Andaman $M_w = 8.7$ megathrust event. Here, instead, we build on the analytical solution for the Burgers' body response to sudden constant stresses, as opposed to a sudden strain. We use this approach because (i) we simulate the entire cycle (slow charge phase followed by sudden discharge) of synthetic earthquakes through a stress ramp (built as a sequence of closely-spaced stepwise stress increases) followed by a sudden stress drop (i.e., a stepwise stress decrease) and because (ii) the focus of this study is on rigid plate motions as sampled from GPS measurements performed sufficiently away from deforming margins (as opposed to near them as in the case of observations of postseismic deformation).

We imagine a plate of area A gliding on top of the viscoelastic asthenosphere at velocity v_0 under the action of a force F_0, which implies a transfer of a shear stress $\sigma_0 = F_0/A$ to the plate-asthenosphere interface. We assume that v_0 is the long-term equilibrium velocity that one would predict under perfectly viscous conditions—that is, v0=DaF0/(μaA)—and take this as initial setting. Let us imagine that at time t_s from the beginning of the thought experiment, such a plate is suddenly subject to a small additional force ΔF_s. By virtue of plate rigidity, an additional sudden shear stress $\Delta\sigma_s = \Delta F_s/A$ (Figure 3a) is transferred to the plate-asthenosphere interface, causing a viscoelastic response. An analytical expression exists for the temporal evolution of strain variation $\Delta\epsilon(t)$ in a Burgers' body upon application of a sudden stress, such as $\Delta\sigma_s$ (e.g., Rimdusit et al., 2011). Its time derivative, which represents the variation of strain-rate—relative to the initial setting before t_s—at the plate-asthenosphere interface, is $\Delta\dot{\epsilon}(t) = \Delta\sigma_s/\mu_a \cdot [1 + e^{-(t-t_s)/T_M}]$. Since the velocity of the thin, uppermost layer of the asthenosphere must coincide with the plate velocity, the strain-rate change can be written as $\Delta\dot{\epsilon}(t) = \Delta v(t)/D_a$. Accordingly, the plate-velocity variation—relative to the initial velocity—is

$$\Delta v(t) = v(t) - v_0 = \frac{D_a}{\mu_a}\frac{\Delta F_s}{A}[1 + e^{-(t-t_s)/T_M}] \cdot S(t, t_s), \tag{22}$$

where the step function $S(t, t_s) = 0$ if $t < t_s$, while $S(t, t_s) = 1$ if $t \geq t_s$. The viscoelastic plate-velocity variation is equal to the variation arising from perfectly viscous conditions—that is, $D_a\Delta F_s/(A\mu_a)$—multiplied by a

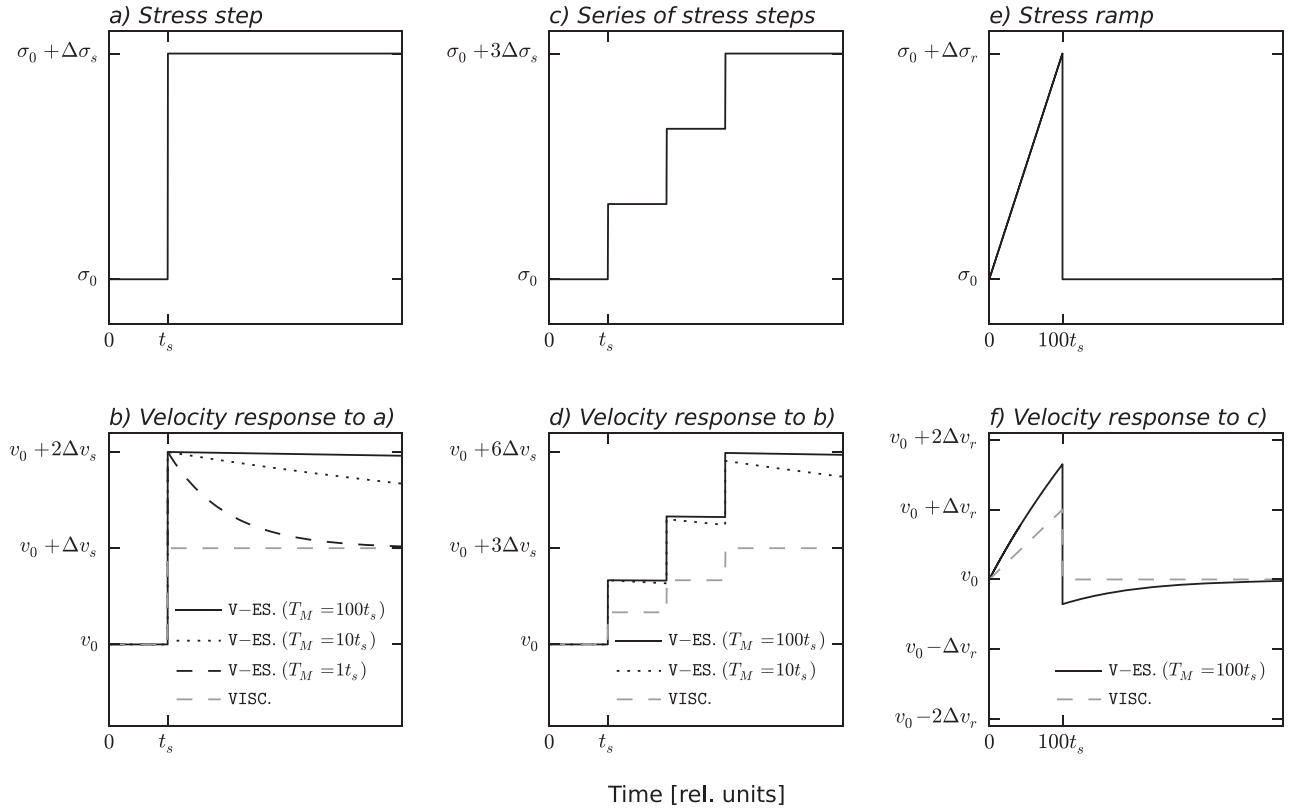

Figure 3. (a) Stress step used in the toy problem (see 2.3.2) and (b) associated plate motion in the perfectly viscous (dashed gray) and three viscoelastic (black) cases. (c,d) Same as (a) and (b) but for a series of three stress steps. (e,f) Same as (a) and (b) but for a stress ramp followed by a sudden stress drop that brings the stress variation back to zero.

function of time and T_M. Figure 3b compares the temporal evolution of the plate velocity when T_M is 1, 10, and 100 times t_s (legend labels `V-ES.`; Figure 3b) with the velocity predicted under perfectly viscous conditions (legend label `VISC.`; Figure 3b). As a consequence of asthenosphere viscoelasticity, the plate velocity increases initially by twice the long-term velocity variation to then decay exponentially toward it. Similarly, a series of three, equally-spaced stress increases by $\Delta\sigma_s = \Delta F_s/A$ (Figure 3c) generates a velocity response that is the superimposition of three responses like the one in Figure 3b but progressively shifted in time (Figure 3d). In such a case, the velocity variation through time can be expressed as

$$\Delta v(t) = \sum_{j=1}^{3} \frac{D_a}{\mu_a} \frac{\Delta F_s}{A} \left[1 + e^{-(t-jt_s)/T_M}\right] \cdot S(t, jt_s). \tag{23}$$

Lastly, let us imagine a cycle of 100 closely-spaced step increases of force by ΔF_s (i.e., a stress ramp), each occurring a short interval of time t_s after the previous one, followed by a sudden force drop equal to $-\Delta F_r = -100\Delta F_s$, which brings the net force variation upon the plate back to zero. The stress variations upon the asthenosphere will then be $+\Delta\sigma_s$ for 100 times, followed by a sudden stress drop equal to $-\Delta\sigma_r = -100\Delta\sigma_s$ (see Figure 3e). The temporal evolution of the plate velocity in response to such a stress cycle, which mimics the one associated with a synthetic earthquake, be expressed analytically as follows:

$$\Delta v(t) = \sum_{j=1}^{100} \frac{D_a}{\mu_a} \frac{\Delta F_r}{100A} \left[1 + e^{-(t-jt_s)/T_M}\right] \cdot S(t, jt_s) - \frac{D_a}{\mu_a} \frac{\Delta F_r}{A} \left[1 + e^{-(t-100t_s)/T_M}\right] \cdot S(t, 100t_s). \tag{24}$$

Figure 3f illustrates the temporal evolution of the plate velocity for the case when $T_M = 100t_s$ and compares it to the velocity obtained under perfectly viscous conditions.

2.3.3. $\Delta\vec{\omega}_e$ Associated With $\Delta\vec{M}_e$—Case of a Viscoelastic Asthenosphere

Equation (21) allows linking torque variations to Euler-vector variations predicted under perfectly viscous conditions in 3-D spherical geometry. $\mathbf{C^{-1}}$ in equation (21) fulfills the same role of $D_a/(\mu_a A)$ in the case

of the toy problem (1-D linear geometry)—the difference by a length squared in the dimensions of the two coefficients simply accounts for the fact that equation (21) concerns torques (instead of forces) and Euler vectors (instead of linear velocities). In the simulations built for this study, the patterns of stress upon the model microplate associated with each synthetic earthquake are the same of that in Figure 3e, with duration and height of the stress ramp determined by the magnitude of each single earthquake, as illustrated above. Torque variations associated with these stresses will follow the same pattern, as described in 2.2. On this bases, as well as on the basis of the result expressed in equation (24), the 3-D spherical viscoelastic Euler-vector variation through time shall be expressed as a summation of terms shifted in time—each term being the product of the 3-D spherical long-term velocity change (i.e., that drawn when assuming a perfectly-viscous asthenosphere) and the time function. Therefore, the microplate Euler-vector variation associated with a synthetic earthquake whose charging phase starts at time t_e through model time is

$$\Delta\vec{\omega}_e(t) = \sum_{j=1}^{(n_e-1)} \frac{\mathbf{C^{-1}}\Delta\vec{M}_e}{n_e-1}\left[1+e^{-\frac{t-(t_e+jt_S)}{T_M}}\right]\cdot S(t,t_e+jt_s) - \mathbf{C^{-1}}\Delta\vec{M}_e\cdot\left[1+e^{-\frac{t-(t_e+n_et_S)}{T_M}}\right]S(t,t_e+n_et_s), \quad (25)$$

where t_s now represents the duration of a model time step, while $\Delta\vec{M}_e$ is obtained combining equations (1), (2), (4), and (7) above. Equation (25) allows us to sample, for all earthquakes in each simulation, the time-dependent microplate Euler vector and its variations through model time at a simulated temporal resolution equal to the model time step.

3. Results From Synthetic Simulations of Microplate Dynamics

We implement the procedures and equations described in Section 2 using Matlab. For each simulation of microplate dynamics, we initially sample the Euler-vector variations through model time at a temporal resolution equal to the model time step. Geodetic estimates of Euler vectors are typically drawn from position time series spanning 3 to 5 yr (e.g., Argus et al., 2010; Bock & Melgar, 2016; England et al., 2016; McClusky et al., 2000; Sella et al., 2002). In order to mimic such a feature, we average the model Euler vector over the appropriate number of time steps that make up for a 3-yr period and take this as a synthetic representation of real geodetic estimates of the microplate motion. In Figure 4, we show the angular velocity time series for one simulation, from the initial model time to the model time interval before the largest earthquake occurs. In red is the time series calculated when we account for all earthquakes, in blue that associated only with the single largest earthquake (for the sake of comparison, the thin, light-blue line shows the same time series but calculated under the assumption of perfectly-viscous behavior of Earth's asthenosphere), while in black that associated with all but the largest earthquake. We elect to consider the kinematic changes arising from the charge of the largest earthquake as the main feature to identify. Instead, we consider the changes arising from all other events as a background signal that may hamper identifying the main variations of the microplate motion. The degree to which the main kinematic pattern associated with the largest earthquake is disrupted by the impact of all other smaller earthquakes is a direct result of the randomness built in our models. On this basis, we try to identify distinctive traits of the main kinematic pattern that may indicate with some confidence the ongoing charge of the largest earthquake.

3.0.1. Impact of Time Series Length

We proceed by imagining that one could estimate the microplate motion through geodetic measurements and thus obtain Euler-vector time series. Such time series may not necessarily start at the beginning of the charge phase of the largest earthquake but could also start afterward. Because of this, we focus on the Euler-vector temporal change relative to the first one available. We build time series for the norm of the difference between the Euler vector through model time and the first one available. Figure 5a shows such calculations for the same simulation of Figure 4, assuming that time series are available from the beginning of model time (in blue), 1/5 into it (in black), 1/2 into it (in magenta), and 4/5 into it (in green). In other words, we simulate scenarios where Euler-vector time series are available for varying periods of model time before the largest earthquake occurs. Thus, the first available estimate of the microplate Euler vector varies from one case to the other.

It makes sense to compare the norm of the Euler-vector variation with the typical confidence range one can expect on geodetically-derived Euler vectors. This allows us to test whether the simulated magnitudes of the changes arising from the charge of the largest earthquake are beyond realistic geodetic uncertainties.

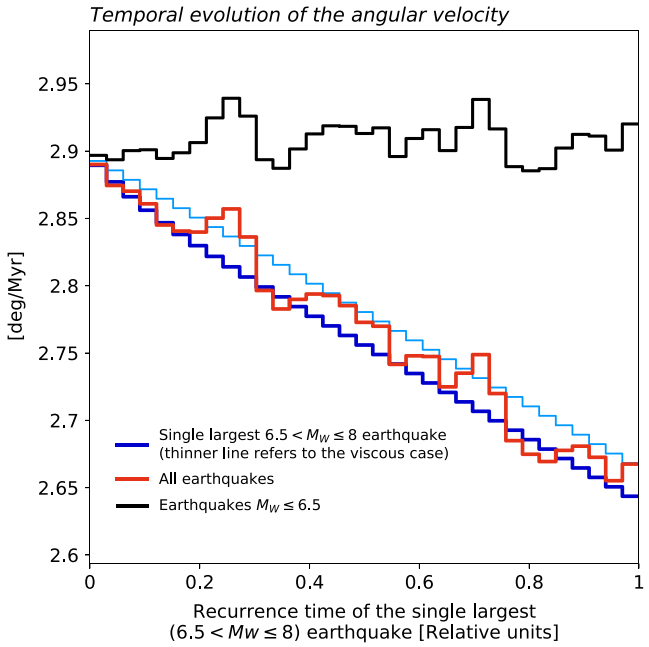

Figure 4. Temporal evolution of the microplate angular velocity through model time from one simulation. Parameter values are $\mu_a = 5 \cdot 10^{19}$ Pa · s, $\mu_m = 1.5 \cdot 10^{21}$ Pa · s. Microplate side length is 550 km.

We resort to the comprehensive study of Argus et al. (2010), who estimated Euler vectors and associated covariance matrices for present-day tectonic plates. We focus on the norm of the diagonals of the covariance matrices, as they provide an indication of the size of the error ellipses around the best-fitting Euler vectors. These are at most $9 \cdot 10^{-3}$°/Myr, which we adopt as confidence range on the synthetic Euler vectors. Thus, the confidence range on the Euler-vector variation (i.e., norm of the difference between two Euler-vector estimates) is at most $2 \cdot 9 \cdot 10^{-3}$°/Myr (gray lines in Figure 5). Results from the simulation in Figure 5a indicate that, regardless of when the available time series begins, the norm of the Euler-vector variation becomes larger than the assumed confidence range—which in the following, we refer to as *threshold*—and remains above it for all of the remaining time. Instead, removing the contribution of the largest earthquake from the Euler-vector time series results in variations that overall fluctuate around the threshold, without remaining above it throughout all or most of the remaining model time (Figure 5b). Such a difference of kinematic behaviors could be seen as a distinctive feature associated with the charge of the largest earthquake. However, the randomness in model time and location of the whole set of synthetic earthquakes implies that such a behavior may not occur as early in model time as it does in Figure 5a or that it may not occur at all. For instance, in Figures 5c and 5d, we show results from a second, different simulation where we observe that the time series of Euler-vector variations exceed the threshold for all or most of the remaining time (Figure 5c vs. Figure 5d), but this does not occur as early as it does in the previous example (Figures 5a and 5b).

We adopt the following as a quantitative way of attempting to identify the charge of the largest earthquake in the Euler-vector variation time series: Once the time series exceeds—not necessarily for the first time—the assumed threshold, we estimate the fraction of remaining model time where the time series maintains itself above such a threshold. We place a stringent condition and request that such a fraction be at least 90% of the remaining time—in the following, we refer to this as *90% criterion*. For instance, all the time series in Figures 5a and 5c meet such a criterion. However, those in Figure 5a do so already after ~0.1 of the remaining model time, while two of the time series in Figure 5c (black and purple lines) do so during the second half of the remaining model time. Instead, almost all the time series that do not account for the impact of the largest earthquake (Figure 5b/5d) do not meet such a criterion. Varying the 90% value effectively means accepting for a longer or shorter period of model time that all other earthquakes may disrupt or possibly overwhelm the kinematic imprint of the largest one. For instance, adopting a 50% value—instead of 90%—would imply that two of the time series in Figure 5d (black and purple) would yield a *false positive*—that is, they would meet the 50% criterion even though the impact of the largest earthquake has been deliberately excluded. On the basis of all the considerations above, we elect to take a statistical approach where we map, through histograms drawn from ensembles of 5,000 repeated simulations, how long does it take to meet the 90% criterion—in the following referred to as *delay*—in three different cases: (i) when the impact of all the earthquakes in the set is accounted for, (ii) when the largest earthquake is excluded from the simulations (i.e., $M_W < 6.5$), and (iii) when taking only $M_W < 5.5$. We do so for varying values of μ_a, μ_m, b value, and microplate size. These calculations provide us with a statistical overview of whether and how rapidly the time series of microplate motions may signal the ongoing charge of the largest earthquake at a confidence level that is determined by realistic uncertainties on Euler-vector estimates, as well as realistic distributions of smaller seismic events in the brittle microplate boundaries.

We proceed by gathering histograms for the delay observed across the ensembles using the 90% criterion. Figure 6 shows the delay histograms for the ensemble featuring $\mu_a = 5 \cdot 10^{19}$ Pa · s and $\mu_m = 1.5 \cdot 10^{21}$ Pa · s, which yield an asthenospheric thickness $D_a = 150$ km. The microplate side length at the surface is 550 km, while the microplate thickness is set to $H_p = 170$ km in order to be consistent with equation (1). In this ensemble, we used $b = 1$. In each panel, a delay equal to 0 corresponds to the beginning of the available time series, which is different from one panel to the other (see panel labels). Instead, a delay equal to 1

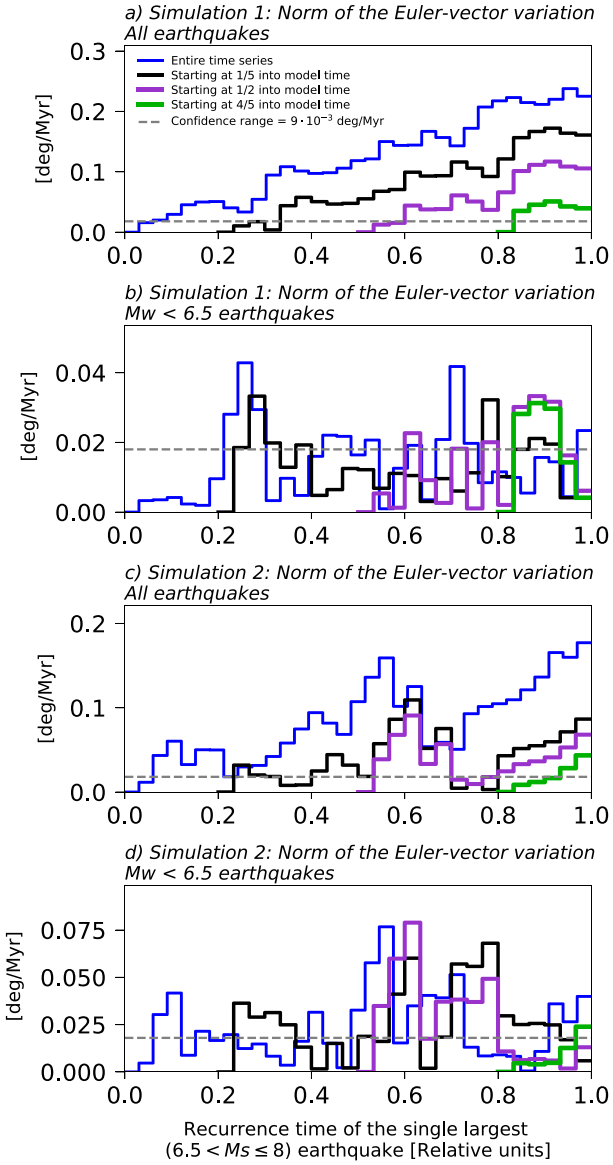

Figure 5. (a) Temporal evolution of the norm of the Euler-vector variation from one simulation, calculated after having assumed that time series are available from the beginning of model time (blue), 1/5 into it (black), 1/2 into it (magenta), and 4/5 into it (green). In gray is the confidence range on synthetic Euler-vector variations, which—following the error propagation rule—is twice the assumed confidence on synthetic Euler-vector estimates (i.e., $9 \cdot 10^{-3^\circ}$/Myr). (b) Same as (a) but not accounting for the impact of the largest earthquake onto microplate motion. (c,d) Same as (a) and (b) but from a second, different simulation.

always corresponds to the time step when the largest earthquake within the synthetic set occurs. Thus, delays in Figure 6a can be anything between 0 and the length of the charge phase of the largest earthquake. Instead, delays in Figure 6c, for instance, can be only between 0 and half that length, since the available Euler-vector time series are assumed to start half way through the charge phase of the largest earthquake. The width of histogram bins is set such that they always corresponds to 1/20 of the charge phase of the largest earthquake. Note that the last bin of each panel counts also those simulations that never meet the 90% criterion. The gray histogram bars refer to simulations where we account for the impact of all synthetic earthquakes ($3.5 \leq M_W \leq 8$) onto the microplate dynamics. Instead, solid-contoured empty bars refer to calculations where we only include the torque variations associated with earthquakes whose $M_W < 6.5$, while dash-contoured empty bars refer to the case where $M_W < 5.5$.

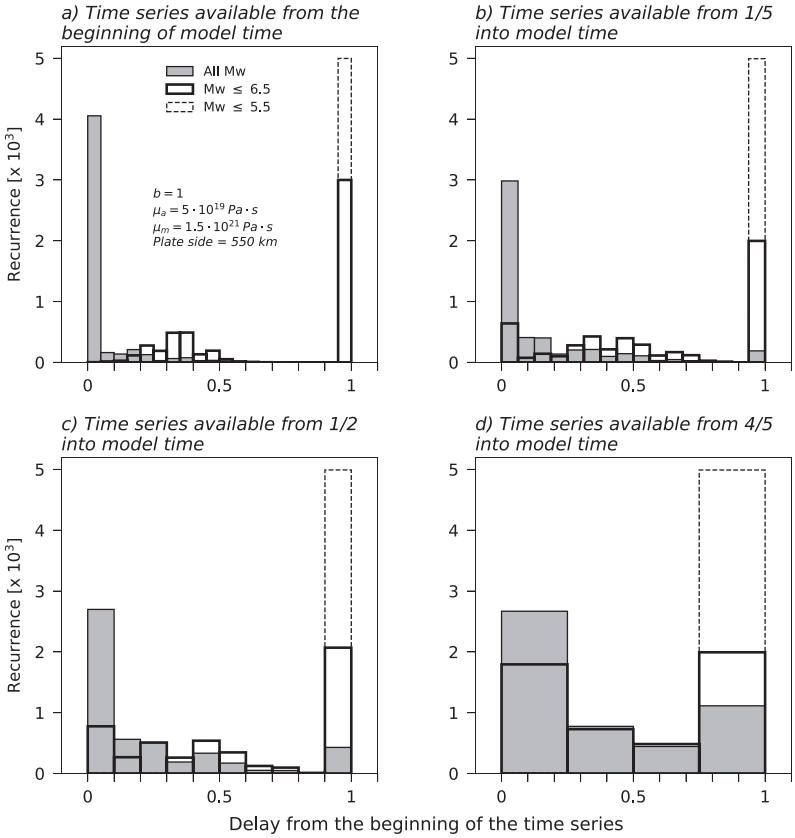

Figure 6. Histograms of the delay observed across ensembles of simulations. Delays are calculated using the 90% criterion (see main text for details) and an assumed confidence range on Euler-vector estimates of $9 \cdot 10^{-3^\circ}$/Myr. (a) Delay histograms calculated assuming that time series of Euler-vector variations are available from the beginning of model time. (b–d) Same as (a) but assuming that time series are available from 1/5, 1/2, and 4/5, respectively, into model time.

In Figure 6a, we present results for the case where synthetic estimates of the microplate Euler vector are assumed to be available from the beginning of the charge phase of the single largest earthquake. The delay for the calculations accounting for all earthquakes is less than 0.05 for ~80% of the sample simulations—that is, around 4,000 samples out of 5,000. This means that already after less than 0.05 of the model time left (until the largest earthquake occurs), most of the synthetic Euler-vector time series have met the 90% criterion. Instead, if one excludes the torque variation associated with the largest earthquake (solid-contoured empty bars), most of the synthetic time series fall into the last bin, while several previous bins—from 0.6 to 0.95—are actually empty. This indicates that most of the synthetic time series actually never meet the 90% criterion. There are some simulations that do (around 2,000 out of 5,000), but we note that these return much longer delays than those in the majority of simulations that do feature the torque variation associated with the largest earthquake—that is, ≤ 0.05. In fact, delays are in range 0.15 to 0.55 and owe to the few earthquakes whose M_W is between 5.5 and 6.5, since simulations not accounting for earthquakes whose $M_W \geq 5.5$ systematically yield a delay ≥0.95 or never meet the 90% criterion (dashed-contoured bars in Figure 6a).

Figures 6b and 6c show histograms from the same ensemble as Figure 6a, but this time assuming that synthetic time series are available starting at 1/5 and 1/2, respectively, into the charge phase of the single largest earthquake. Accounting for the torque variations associated with all earthquakes in the set yields results that are similar to those of Figure 6a—that is, most of the simulations feature short delays (less than ~0.1). Similarly, the majority of the simulations that do not account for the impact of the largest earthquake either feature a delay ≥0.9 or never meet the 90% criterion. However, this time there are some simulations yielding delays shorter that ~0.1—around 700 out of 5,000 in Figure 6b and around 800 out of 5,000 in Figure 6c. This is because synthetic time series start when the largest earthquake is already charging, and thus, the remaining model time available for the main kinematic signal to exceed and remain above the threshold is

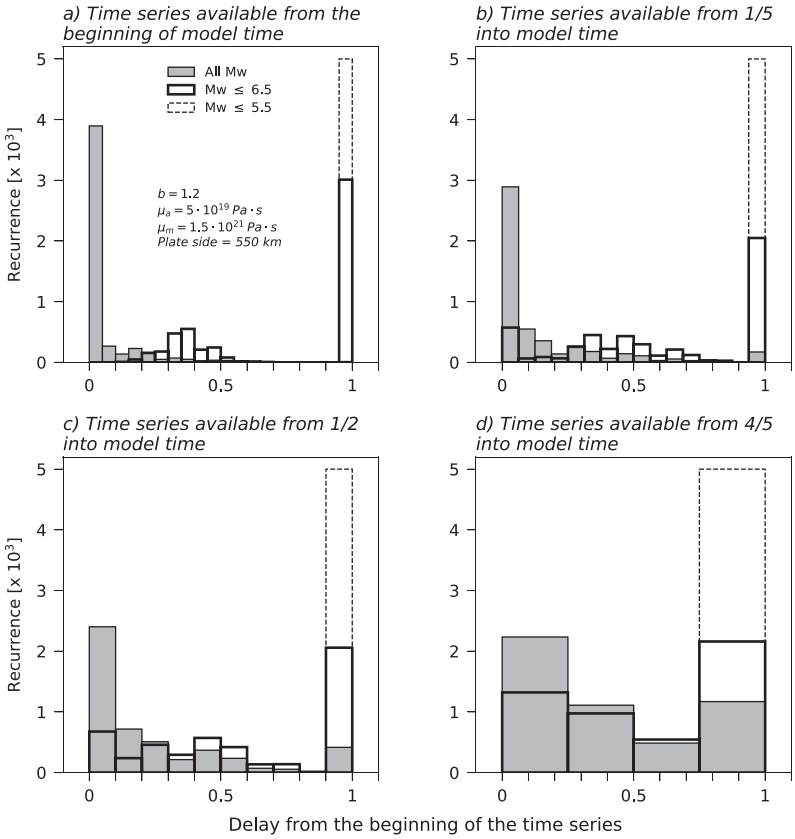

Figure 7. Same as Figure 6 but this time using $b = 1.2$.

less. In other words, smaller earthquakes have a higher chance to disrupt and possibly overwhelm the main signal, making it fluctuating around the threshold. Figure 6d shows results for time series starting toward the final stages of the largest earthquake charge phase—that is, only 1/5 of remaining model time before it occurs. In this case, histograms show very similar patterns, regardless of whether we account or not for the impact of the largest earthquake charge. This means that time series are too short—that is, they start too late through model time—to link with some statistical confidence their temporal variations to the charge of the largest earthquake.

Taken altogether, results in Figure 6 indicate that the length of the available time series has a bearing on making efficient use of time series of microplate-motion variations in order to highlight—in a statistical fashion and with some confidence—the charge phase of the largest earthquake. The longer the time series are, the higher is the chance that meeting the 90% criterion relatively early through model time is a feature linked with significant probability (see Figures 6a–6c) to the charge phase of the largest earthquake, as opposed to kinematic changes caused by smaller earthquakes—that is, $5.5 \leq M_W < 6.5$ (see Figure 6d). This can be interpreted as follows: Torque variations generated by the charge phase of the single largest earthquake impact on the microplate motion slowly but systematically in the same direction. They compete against (i) contributions from smaller earthquakes that meanwhile occur more frequently, as well as (ii) resistive stresses at the base of the microplate. If such a competition occurs for longer time, it is more likely that the time-integrated torque associated with the slow charge phase of the single largest earthquake changes the microplate motion almost systematically beyond the confidence associated with Euler vector estimates.

3.0.2. Impact of *b* Value

Next, we explore the impact of the Gutenberg-Richter parameter b on the delay histograms. One could anticipate that the same inferences illustrated above would hold for $b < 1$. This is because the synthetic set of earthquakes would feature fewer smaller earthquakes that hamper the main microplate-motion variations associated with the charge phase of the single largest earthquake. In supporting information S1, we verify that this is the case. Instead, it is more interesting to explore here the scenario arising from earthquake synthetic sets generated using $b > 1$. Figure 7 shows delay histograms drawn from ensembles whose parameters

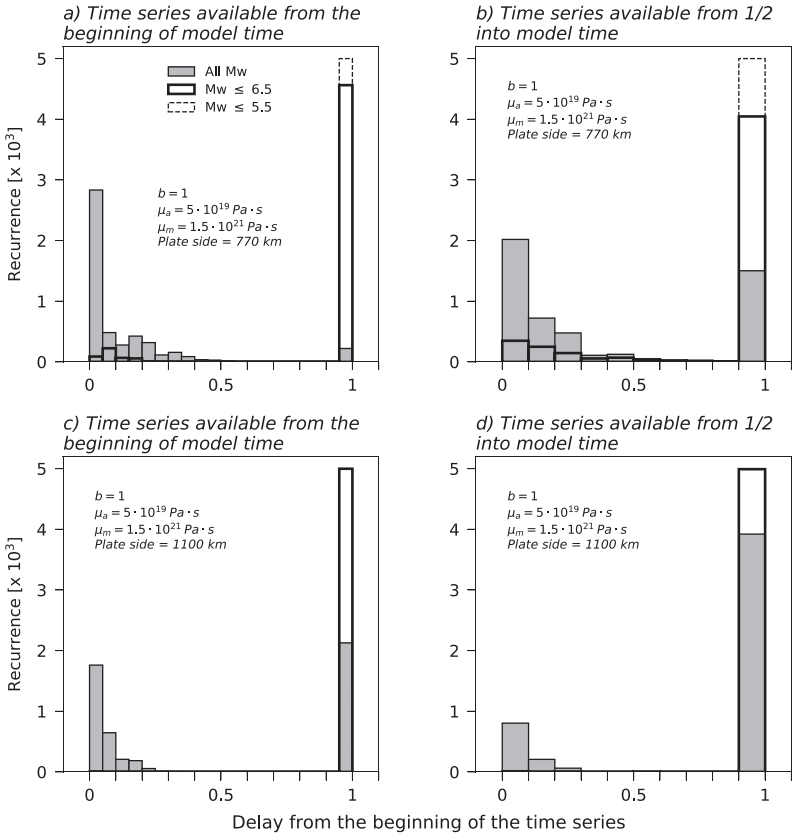

Figure 8. (a/b) Same as Figure 6a/6c but this time using a length of the plate side equal to 770 km. (c/d) Same as Figure 6a/6c but this time using a length of the plate side equal to 1,100 km. Other parameter values are also reported.

are the same of those in Figure 6, except for b that is now set to 1.2. Despite the fact that these ensembles feature a total of $int[10^{(3\cdot1.2)}] = 3,981$ earthquakes—as opposed to the 1,000 events associated with $b = 1$—it is evident that the inferences drawn above still hold.

3.0.3. Impact of Plate Size and μ_a

Next, we reevaluate the scenario in Figure 6a/6c, where we assumed that time series are available from the beginning of the charge phase of the largest earthquake and from 1/2 into it, varying one other parameter at a time. First, we explore the impact of varying the microplate size. In Figures 8a and 8b, we repeat the same analysis of Figure 6a/6c, this time for a microplate whose plate-side length is 770 km, as opposed to 550 km. Such a parameter variation implies virtually no significant change in the magnitudes of the torque variations associated with earthquakes, because rupture areas and torque arms do not vary. However, the microplate basal area, which hosts resistive shear stresses, increases by a factor of ~2. This means that larger torques now act against virtually the same torque variations arising from the set of synthetic earthquakes. In Figures 8a and 8b, we can observe that the majority of the simulations that exclude the largest earthquake ($M_W \leq 6.5$) do not meet the 90% criterion, as the torques associated to earthquakes whose magnitude is in range $5.5 < M_W < 6.5$ are not large enough to overcome the viscous resistance at the base of the plate. However, our ability to point toward the charge phase of the largest earthquake still hold with confidence. In Figures 8c and 8d, we increase the plate-side length to 1,100 km, which is an upper limit for the size of present-day microplates (e.g., Wallace et al., 2005). In this case, the basal area is ~4 times the basal area for a microplate with a side length of 550 km. Although some simulations meet the 90% criterion (around 2,800 in Figure 8c and 1,200 in Figure 8d), there are many that do not, indicating that the ability of the torque variations arising from the charge of the single largest earthquake to impact on the microplate rigid motion is somewhat compromised when considering microplates of the size of a small tectonic plate (i.e., 10^6 km^2). In Figures 9a and 9b, we explore the impact of changing the viscosities of the asthenosphere and the lower upper mantle. From the histograms associated with ensembles of simulations where μ_a increases to 10^{20} Pa · s, it is evident that results resemble those of Figure 6a/6c, indicating that the previous inferences

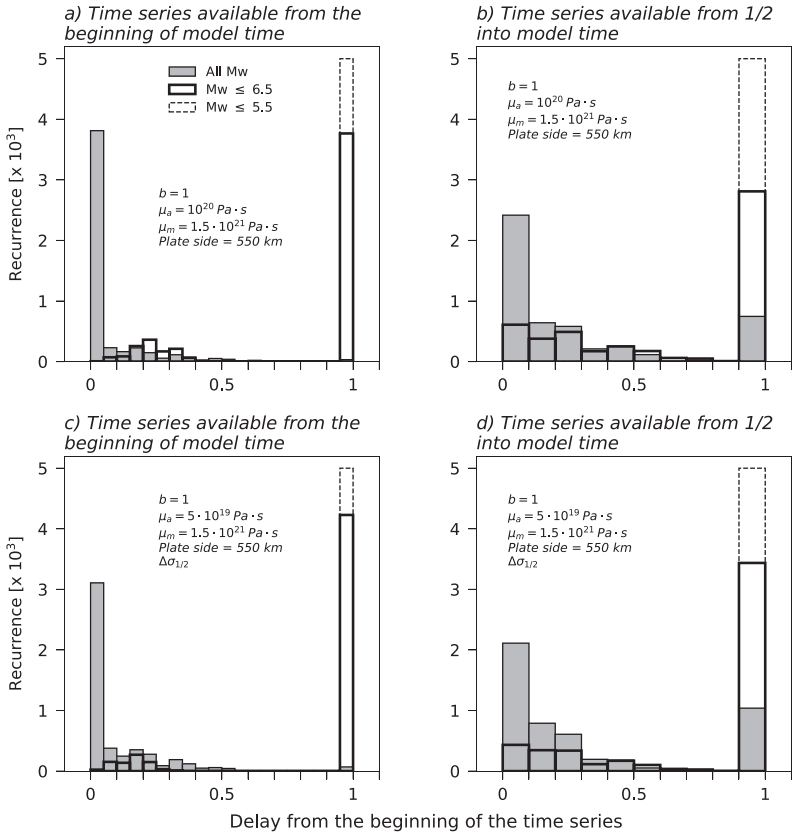

Figure 9. (a/b) Same as Figure 6a/6c but this time using $\mu_a = 10^{20}$ Pa · s. (c/d) Same as Figure 6a/6c but this time assuming that only half of the stress drop that is linearly built along the faults is converted into a torque change. Other parameter values are also reported.

hold when increasing the asthenospheric viscosity value to a realistic upper limit. In supporting information S1, we draw similar inferences from histograms related to ensembles of simulations where $\mu_m = 4{\cdot}10^{21}$ Pa·s.

4. Discussion and Conclusions

It is worth discussing some of the assumptions we make in the simulations: (i) We implemented the notion that the stresses accrued along future rupture areas are fully released during the associated synthetic earthquakes. This is in line with findings from a variety of studies on the effective coefficient of friction along large-scale faults (e.g., Bird, 1998; Iaffaldano, 2012; Suppe, 2007), which indicate that friction coefficients typically do not exceed 0.1. This means that the stress drops during earthquakes are essentially equal to the stress levels accrued before seismic events. Furthermore, (ii) we also assumed that all of the stress accrued during the charge phase contributes to a torque change that impacts on the microplate rigid motion. In other words, we neglected that a fraction of such a growing stress may be spent on elastic deformation near parts of the microplate margins. Lastly, (iii) we assumed that the stresses built along the microplate margins during the charge phases do not depend on the slip rate. While we are aware that this is an approximation, we note that the dependence of the plate-interface strength on slip velocity in the brittle part of plate margins—which hosts up to 80% of the depth-integrated strength (e.g., Iaffaldano, 2012)—has been inferred from laboratory experiments to be relatively weak (e.g., Di Toro et al., 2011; Kohlstedt et al., 1995) at slip rates comparable to those in place during the charge phase. Quantifying exactly the relative contributions of these processes is beyond the goals of this feasibility study. However, a rudimental assessment of the impact that these processes could have on the kinematic patterns observed in the tests presented here is the following: In Figures 9c and 9d we reevaluate the analysis of Figure 6a/6c, but this time assuming that only half of the stress accrued during the charge phase actually impacts onto the microplate rigid motion, while the other half is assumed not to (because it may be taken up, for instance, by crustal deformation along the microplate margins). Under these circumstances, few of the simulations not accounting for the presence of

the single largest earthquake (solid-contoured empty bars) do meet the 90% criterion. However, the statistical inference that meeting the 90% criterion with short delay is an indication of the charge phase of the largest earthquake still holds with confidence. We emphasize that the results in Figures 9c and 9d should be seen as a very first-order way of assessing whether the inferences presented in Section 3 hold despite the simplifications listed above.

The synthetic tests reported here indicate that the charge phase of large earthquakes (e.g., $M_W \geq 6.5$) shall expected to impact on the temporal evolution of microplates rigid motions in a way that leaves an early signature. This happens for realistic values of the abovementioned parameters and despite the occurrence of smaller earthquakes in the background. On this basis, we conclude that it appears feasible to link with some confidence the temporal changes of geodetically observed microplate motions to the charge phase that preludes to large earthquakes.

Acknowledgments
All data and methods used in this study come from referenced sources, are described herein, or a publicly available on a repository (https://sid.erda.dk/sharelink/CEvpHlsMMQ). Authors are grateful to the editor (Paul Tregonning), the associate editor, Rob Govers, and an anonymous reviewer for constructive comments that improved the manuscript. J. M. B. acknowledges support from a fellowship (LCF/BQ/EU17/11590058) from La Caixa banking foundation (ID 100010434), as well as support from the Department of Geosciences and Natural Resource Management at the University of Copenhagen. G. I. acknowledges support by a research grant (00023121) from VILLUM FONDEN.

References

Argus, D. F., Gordon, R. G., Heflin, M. B., Ma, C., Eanes, R. J., Willis, P., & Owen, S. E. (2010). The angular velocities of the plates and the velocity of Earth's centre from space geodesy. *Geophysical Journal International*, *180*, 913–960.

Ben-Zion, Y. (2008). Collective behavior of earthquakes and faults: Continuum-discrete transitions, progressive evolutionary changes, and different dynamic regimes. *Reviews of Geophysics*, *46*, RG4006. https://doi.org/10.1029/2008RG000260

Bird, P. (1998). Testing hypotheses on plate–driving mechanisms with global lithosphere models including topography, thermal structure, and faults. *Journal of Geophysical Research*, *103*, 10115–10129.

Bock, Y., & Melgar, D. (2016). Physical applications of GPS geodesy: A review. *Reports on Progress in Physics*, *76*, 106801.

Bourne, S. J., Arnadottir, T., Beavan, J., Darby, D. J., England, P. C., Parsons, B., & Wood, P. R. (1998). Crustal deformation of the Marlborough fault zone in the South Island of New Zealand: Geodetic constraints over the interval 1982–1994. *Journal of Geophysical Research*, *103*, 30,147–30,165.

Broerse, T., Riva, R., Simons, W., Govers, R., & Vermeersen, B. (2015). Postseismic GRACE and GPS observations indicate a rheology contrast above and below the Sumatra slab. *Journal of Geophysical Research: Solid Earth*, *120*, 5343–5361.

Bunge, H. P. (2005). Low plume excess temperature and high core heat flux inferred from non-adiabatic geotherms in internally heated mantle circulation models. *Physics of the Earth and Planetary Interiors*, *153*(1-3, SI), 3–10. https://doi.org/10.1016/j.pepi.2005.03.017

Dal Zilio, L., van Dinther, Y., Gerya, T., & Pranger, C. (2018). Seismic behaviour of mountain belts controlled by plate convergence rate. *Earth and Planetary Science Letters*, *482*, 81–92.

Davies, G. F. (1999). *Dynamic earth: Plates, plumesand mantle convection*. Cambridge, United Kingdom: Cambridge University Press.

Di Toro, G., Han, R., Hirose, T., De Paola, N., Nielsen, S., Mizoguchi, K., & Shimamoto, T. (2011). Fault lubrication during earthquakes. *Nature*, *471*, 494–498.

Dixon, T. H. (1991). An introduction to the Global Positioning System and some geological applications. *Reviews of Geophysics*, *29*, 249–276.

England, P., Houseman, G., & Nocquet, J. M. (2016). Constraints from GPS measurements on the dynamics of deformation in Anatolia and the Aegean. *Journal of Geophysical Research: Solid Earth*, *121*, 8888–8916. https://doi.org/10.1002/2016JB013382

Forte, A. M., Quere, S., Moucha, R., Simmons, N. A., Grand, S. P., Mitrovica, J. X., & Rowley, D. B. (2010). Joint seismic-geodynamic-mineral physical modelling of African geodynamics: A reconciliation of deep-mantle convection with surface geophysical constraints. *Earth and Planetary Science Letters*, *295*(3-4), 329–341. https://doi.org/10.1016/j.epsl.2010.03.017

Freed, A. M., Bürgmann, R., Calais, E., Freymueller, J., & Hreinsdóttir, S. (2006). Implications of deformation following the 2002 Denali, Alaska, earthquake for postseismic relaxation processes and lithospheric rheology. *Journal of Geophysical Research*, *111*, B01401. https://doi.org/10.1029/2005JB003894

Godano, C., Lippiello, E., & de Arcangelis, L. (2014). Variability of the b value in the Gutenberg–Richter distribution. *Geophysical Journal International*, *199*, 1765–1771.

Gordon, R. G. (1998). The plate tectonic approximation: Plate nonrigidity, diffuse plate boundaries, and global plate reconstructions. *Annual Review of Earth and Planetary Science*, *26*, 615–642.

Govers, R., Furlong, K., van de Wiel, L., Herman, M., & Broerse, T. (2018). The geodetic signature of the earthquake cycle at subduction zones: Model constraints on the deep processes. *Reviews of Geophysics*, *56*, 6–49. https://doi.org/10.1002/2017RG000586

Gutenberg, B., & Richter, C. (1944). Frequency of earthquakes in California. *Bulletin of the Seismological Society of America*, *34*, 185–188.

Iaffaldano, G. (2012). The strength of large-scale plate boundaries: Constraints from the dynamics of the Philippine Sea plate since ∼5 Ma. *Earth and Planetary Science Letters*, *357–358*, 21–30.

Iaffaldano, G. (2014). A geodynamical view on the steadiness of geodetically–derived rigid plate–motions over geological time. *Geochemistry, Geophysics, Geosystems*, *15*, 238–254. https://doi.org/10.1002/2013GC005088

Iaffaldano, G., & Bunge, H. P. (2015). Rapid plate motion variations through geological time: Observations serving geodynamic interpretation. *Annual Review of Earth and Planetary Sciences*, *43*(1), 571–592. https://doi.org/10.1146/annurev-earth-060614-105117

Kanamori, H. (1978). Quantification of great earthquakes. *Tectonophysics*, *49*, 207–212.

Kohlstedt, D. L., Evans, B., & Mackwell, S. J. (1995). Strength of the lithosphere: Constraints imposed by laboratory experiments. *Journal of Geophysical Research*, *100*, 17587–17602.

LaFemina, P., Dixon, T., Govers, R., Norabuena, E., Turner, H., Saballos, A., & Strauch, W. (2009). Fore-arc motion and Cocos Ridge collision in Central America. *Geochemistry, Geophysics, Geosystems*, *10*, Q05S14. https://doi.org/10.1029/2008GC002181

McClusky, S., Balassanian, S., Barka, A., Demir, C., Ergintav, S., Georgiev, I., & Veis, G. (2000). Global Positioning System constraints on plate kinematics and dynamics in the eastern Mediterranean and Caucasus. *Journal of Geophysical Research*, *105*, 5695–5719.

Meade, B. J., & Loveless, J. P. (2017). Block motion changes in Japan triggered by the 2011 great Tohoku earthquake. *Geochemistry, Geophysics, Geosystems*, *18*, 2459–2466. https://doi.org/10.1002/2017GC006983

Nishikawa, T., & Ide, S. (2014). Earthquake size distribution in subduction zones linked to slab buoyancy. *Nature Geoscience*, *7*, 904–908.

Paulson, A., & Richards, M. A. (2009). On the resolution of radial viscosity structure in modelling long-wavelength postglacial rebound data. *Geophysical Journal International*, *179*(3), 1516–1526. https://doi.org/10.1111/j.1365-246X.2009.04362.x

Pollitz, F., Bürgmann, R., & Banerjee, P. (2006). Post-seismic relaxation following the great 2004 Sumatra-Andaman earthquake on a compressible self-gravitating Earth. *Geophysical Journal International*, *167*, 397–420.

Reilinger, R., McClusky, S., Vernant, P., Lawrence, S., Ergintav, S., Cakmak, R., & Karam, G. (2006). GPS constraints on continental deformation in the Africa-Arabia-Eurasia continental collision zone and implications for the dynamics of plate interactions. *Journal of Geophysical Research*, *111*, B05411. https://doi.org/10.1029/2005JB004051

Richards, M. A., & Lenardic, A. (2018). The Cathles Parameter (Ct): A geodynamic definition of the asthenosphere and implications for the nature of plate tectonics. *Geochemistry, Geophysics, Geosystems*, *19*, 4858–4875. https://doi.org/10.1029/2018GC007664

Rimdusit, S., Wongsongyot, S., Jittarom, S., & Tiptipakorn, P. S. S. (2011). Effects of gamma irradiation with and without compatibilizer on the mechanical properties of polypropylene/wood flour composites. *Journal of Polymer Research*, *18*, 801–809.

Rui, X., & Stamps, D. S. (2019). A geodetic strain rate and tectonic velocity model for China. *Geochemistry, Geophysics, Geosystems*, *20*, 1280–1297. https://doi.org/10.1029/2018GC007806

Savage, J. C., & Prescott, W. H. (1978). Asthenosphere readjustment and the earthquake cycle. *Journal of Geophysical Research*, *83*, 3369–3376.

Scholz, C. H. (2019). *The mechanics of earthquakes and faulting*. Cambridge: Cambridge University Press.

Sella, G. F., Dixon, T. H., & Mao, A. (2002). REVEL: A model for recent plate velocities from space geodesy. *Journal of Geophysical Research*, *107*, 2081.

Shen, Z., Jackson, D. D., & Ge, X. (1996). Crustal deformation across and beyond the Los Angeles Basin from geodetic measurements. *Journal of Geophysical Research*, *101*, 27957–27980.

Stein, S., & Wysession, M. (2003). *An introduction to seismology, earthquakes, and earth structure*. Malden, MA: Blackwell Publishing.

Stotz, I. L., Iaffaldano, G., & Davies, D. R. (2018). Pressure-driven Poiseuille flow: A major component of the torque-balance governing Pacific plate motion. *Geophysical Research Letters*, *45*, 117–125. https://doi.org/10.1002/2017GL075697

Suppe, J. (2007). Absolute fault and crustal strength from wedge tapers. *Geology*, *35*(12), 1127–1130.

Symithe, S., Calais, E., de Chabalier, J., Robertson, R., & Higgins, M. (2015). Current block motions and strain accumulation on active faults in the Caribbean. *Journal of Geophysical Research: Solid Earth*, *120*, 3748–3774. https://doi.org/10.1002/2014JB011779

Tormann, T., Enescu, B., Woessner, J., & Wiemer, S. (2015). Randomness of megathrust earthquakes implied by rapid stress recovery after the Japan earthquake. *Nature Geoscience*, *8*, 152–158.

Tregoning, P. (2002). Plate kinematics in the western Pacific derived from geodetic observations. *Journal of Geophysical Research*, *107*, ECV 7–1-ECV 7-8.

Turcotte, D., & Schubert, G. (2002). *Geodynamics*. Cambridge, UK: Cambridge University Press.

Wallace, L. M., McCaffrey, R., Beavan, J., & Ellis, S. (2005). Rapid microplate rotations and backarc rifting at the transition between collision and subduction. *Geology*, *33*, 857–860.

Wallace, L., Stevens, C., Silver, E., McCaffrey, R., Loratung, W., Hasiata, S., & Taugaloidi, J. (2004). GPS and seismological constraints on active tectonics and arc–continent collision in Papua New Guinea: Implications for mechanics of microplate rotations in a plate boundary zone. *Journal of Geophysical Research*, *109*, B05404. https://doi.org/10.1029/2003JB002481